REGULARITIES OF STRUCTURE FORMATION AND PROPERTIES OF COMPOSITE MATERIALS BASED ON ALUMINUM–MANGANESE BRONZE PRODUCED BY ELECTRON BEAM ADDITIVE MANUFACTURING WITH THE ADDITION OF IRON, NICKEL, AND TUNGSTEN POWDERS DURING PRINTING

V. R. Utyaganova, A. V. Chumaevskii, N. N. Shamarin, E. N. Moskvichev,   UDC 539.25
A. V. Vorontsov, D. A. Gurianov, E. O. Knyazhev, and N. L. Savchenko

In the present work, two types of composite materials obtained using electron beam additive manufacturing of aluminum bronze and mixtures of Fe–Ni *and* Fe–W *powders have been studied. Methods of metallographic analysis show relatively uniform distribution of strengthening phases in the volume of products with the presence of only a small number of agglomerates. Mechanical properties of samples are at a sufficiently high level compared to the properties of pure bronze* $CuAl_9Mn_2$. *Microhardness of the surface layers of composites increase up to a factor of 1.5 in comparison with the raw metal. Tribological properties in a set of parameters of mass and linear wear are higher at the composite material with addition of* Fe–W *powder mixture. Friction coefficient of composite samples of both types is at the same level.*

Keywords: additive manufacturing, aluminum–manganese bronze, metal matrix composites, microstructure, x-ray phase analysis, mechanical properties, wear resistance.

INTRODUCTION

Additive manufacturing of metallic materials is a promising technology due to its high productivity and efficiency in the aerospace, automotive, oil, gas and other industries [1–3]. Additive technologies are based on layer-by-layer formation of the part with complex geometry and optimization of its composition and properties for a specific function. There are many different approaches to additive manufacturing of metallic materials, which are divided by the type of filament feed (powder, wire, or rod) and the heat source (laser beam, electric arc, or electron beam) [4, 5]. Powder technologies, such as selective laser fusion, are well suited for obtaining products with a fine internal structure and surface topography. Wire technology is more economical and productive [6]. The combination of wire filament feeding and powder material feeding in electron-beam additive technology makes it possible to combine the positive aspects of both methods of material feeding. This can be used for obtaining products for various applications, including increasing tribological properties of the material [3]. For such purposes, electron-beam additive manufacturing (EBAM) is also one of the most suitable ones, since it allows obtaining parts with a rather smoothly changing structure and properties in the near-surface layers.

Aluminum bronze is an important material due to its high strength and wear resistance [7]. Aluminum bronze is widely used in various parts in the marine industry, such as propellers of ships, rods, and valve nuts [8, 9]. These parts must have high strength and wear resistance for a long service life. However, in a number of applications in industrial production, higher parameters of wear resistance of parts are needed, even from such materials as aluminum bronzes.

TABLE 1. Grade Composition of AISI 321 Alloy and CuAl$_9$Mn$_2$ Alloy

Material	Chemical composition, wt.%										
	Fe	Cu	Cr	Ni	Al	Mn	Ti	C	Si	Zn	Sn
AISI 321 (substrate)	base	<0.3	17–19	9–11	–	< 2.0	0.4–1.0	<0.12	0.8	–	–
CuAl$_9$Mn$_2$ (wire)	<0.5	base	–	–	8–10	1.5– 2.5	–	–	<0.1	<1	<0.1

A possible solution to the problem of increasing the wear resistance of parts may be to obtain composite materials on the basis of aluminum bronze. In [10] it was shown that the application of nickel to aluminum bronze increases the hardness and reduces the wear rate of the resulting composite material, and the results of energy dispersive x-ray analysis show the presence of AlNi$_3$ and AlNi phases. In [11] it was shown that the alloying of the aluminum bronze based alloy with 4% iron increases the mechanical properties and wear resistance, and the alloy wear resistance decreases significantly when the Fe content exceeds 4 %. In [12] an attempt was made to obtain a composite material based on a heat-resistant nickel alloy and aluminum bronze, which has increased hardness, strength, and wear resistance compared to printed bronze. The results of this work show the high efficiency of additive technology to improve the wear resistance of aluminum bronze. Both nickel and iron and tungsten can be effective components for increasing tribological properties of bronzes. Mixtures of these powders deserve special attention. However, the process of obtaining composite materials based on aluminum bronze and powders of iron, tungsten, and nickel, especially in Fe–Ni and Fe–W compositions, by electron beam wire-powder additive method has not been studied so far. The aim of this work is to obtain and study the macro- and microstructure, phase composition, and mechanical and tribological properties of samples based on aluminum bronze and Fe–Ni and Fe–W powder mixtures obtained by electron-beam additive manufacturing.

MATERIALS AND METHODS

The composite samples were obtained on a laboratory electron-beam additive manufacturing setup. The printing scheme is shown in Fig. 1. Printing was performed on the substrate of stainless steel AISI 321 on which CuAl$_9$Mn$_2$ wire was deposited layer-by-layer. The chemical composition of the substrate and wire is given in Table 1.

After printing the thick-walled product (up to ~9 mm), subsequently, composite samples *1* were obtained by feeding powder and wire mixtures from feeders *3* and *4* into melt bath *2* and melting the material by electron beam *5* through magnetic focusing system *6* from gun *7* (Fig. 1). Printing modes of composite materials are presented in Table 2.

The composition of the employed powder mixtures and their mass per printed layer are presented in Table 3. After printing, the samples were cut out for mechanical tests *8* and *9*, tribological tests *10* and *11*, structural studies *12*, and x-ray structural analysis *13* and *14* (Fig. 1).

Samples for structural studies were cut perpendicular to the printing direction and made by grinding, polishing with diamond paste, and suspension. The etching was carried out in a solution of the composition 30 ml HCl + 5 g FeCl$_3$ + 60 ml H$_2$O for 20 s. An optical confocal microscope (Olympus Scientific Solutions Americas, the United States) and an Apreo II SEM FEI scanning electron microscope (Thermo Fisher Scientific, the United States) equipped with an OctaneElectSuper (EDAX) energy dispersive spectral analysis (EDS/EDS) detector were used to study microstructure. X-ray transient absorption (XTA) structural analysis was used to identify phases using an x-ray diffractometer DRON-7 (Burevestnik, Russia) at CoKα radiation. X-ray radiographs were obtained at two levels of the printed composites: from the area of the first layers printed with powder and from the upper area of the composite to analyze the distribution of the phases present.

Vickers microhardness was determined using a Duramin-500 hardness tester (Struers A/S, Ballerup, Danemark) with a load of 50 g. A universal testing machine (Testsystems, Russia) was used for tensile tests at room

TABLE 2. Print Mode of Composite Materials by the EBAM Method

Filament	Wire diameter	Accelerating voltage, kV	Electron beam current, mA	Printing velocity, mm/min
Wire	1.6	30	40	380
Powder	–		37	100

TABLE 3. Ratio of Initial Powder Mixtures and Their Weight per Printed Layer in EBAM Printing

Powder mixture	Chemical composition, wt.%			Mass of the powder mixture per printed layer, g
	W	Ni	Fe	
1	–	50	50	2.0
2	50	–	50	3.0
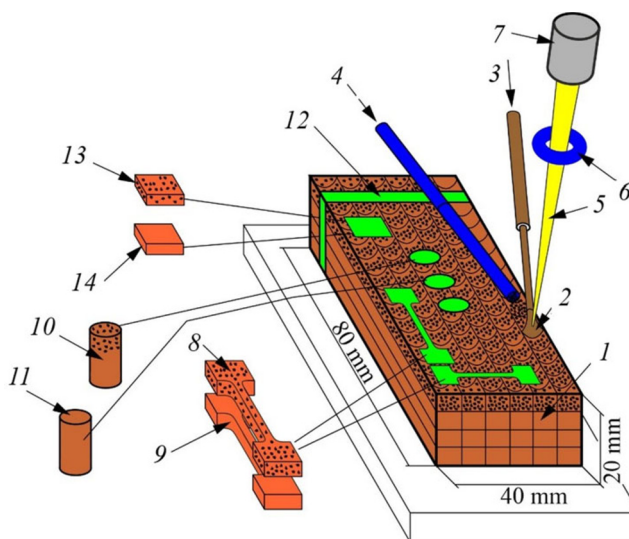
Fig. 1. Scheme of composite printing by the EBAM method and cutting out metallographic sections and specimens for mechanical and tribological tests comprising sample *1*, melt bath *2*, wire feeder *3*, powder feeder *4*, electron beam *5*, focusing system *6*, electron gun *7*, samples *8* and *9* for mechanical tests, samples *10* and *11* for tribological tests, samples *12* for metallographic tests and microhardness measurements, and samples 13 and *14* for x-ray analysis.

temperature. The tensile speed was 1 mm/min. Microhardness measurements of the two tracks were performed in the cross section perpendicular to the direction of composite printing.

The friction tests were carried out on a tribotester using the finger-disc scheme. Finger specimens in the form of cylinders with a length of ~13 mm were prepared from composite material. AISI 420 steel was used as a counterbody. The following parameters were chosen for the test: load 15 N, friction radius 10 mm, speed 500 rpm, and time 2 h. The mass and linear dimensions (length) were measured to determine the amount of wear before and after the test.
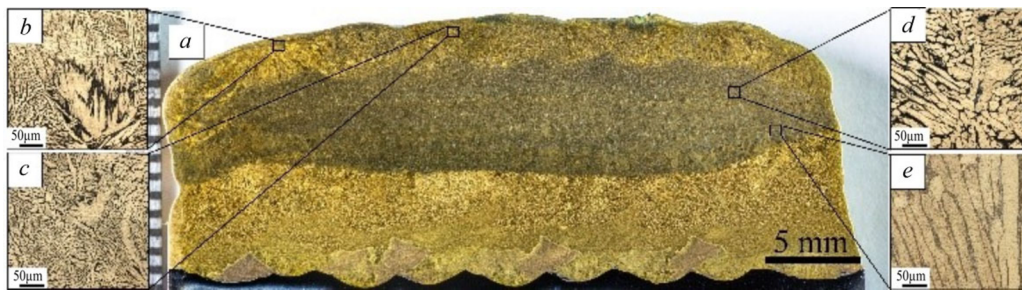
Fig. 2. Structure of the composite based on $CuAl_9Mn_2$ bronze with addition of Fe and Ni powder mixture obtained by the EBAM method: *a* – general view of the sample cross section, and *b–e* – metallographic images of different areas of the composite.
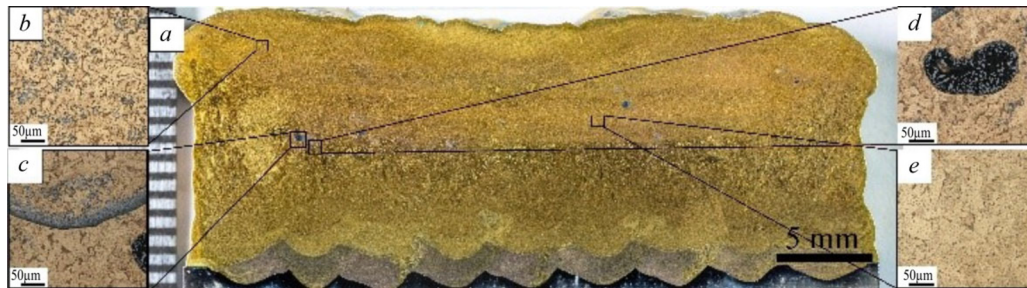

Fig. 3. Structure of the composite based on $CuAl_9Mn_2$ bronze with addition of Fe and W powder mixture obtained by EBAM method: *a* – general view of the sample cross section, and *b–e* – metallographic images of different areas of the composite.

RESULTS AND DISCUSSION

The macro- and microstructure of the samples $CuAl_9Mn_2$ + Fe–Ni (Fig. 2) and $CuAl_9Mn_2$ + Fe–W (Fig. 3) cut in the cross section perpendicular to the printing direction obtained by EBAM demonstrates the absence of large defects like pores, cracks, or delaminations. In both cases, a transition layer of ~2 mm was formed near the steel substrate. In the printed $CuAl_9Mn_2$ alloy with an extension of 5 ± 1 mm, the formation of dendritic columnar α-Cu grains is observed (Figs. 2*a* and 3*a*).

The structure of the $CuAl_9Mn_2$ + Fe–Ni composite is rather homogeneous and consists of columnar α-Cu dendritic grains the length and thickness of which decrease with increasing height of the printed product (Fig. 2*b–d*). The β`-phase is formed along the grain boundaries, as described in work [13].

The top part of the product in the sample $CuAl_9Mn_2$ + Fe–W is represented by dendritic grains of copper with particles of unmelted Fe–W powder (Fig. 3*b*). The structure of the middle part of the composite is represented by areas of large powder agglomerates (Fig. 3*d* and *c*) embedded in the bronze matrix. Fig. 3*e* shows the homogeneous structure consisting of columnar α-Cu grains. The results of the XRF analysis are shown in Fig. 4. In both cases (Fig. 4*a* and *b*), when the powder mixture was added to the bronze, no new phases were detected by XRD.

In the case of the $CuAl_9Mn_2$ + Fe–Ni composite with addition of a mixture of iron and nickel powders, the ferritic iron phase was detected in addition to the FCC lattice reflexes of copper, while nickel was completely dissolved in the copper matrix, and no reflections from the nickel crystal lattice were detected. The α-Fe content averaged 7.1 ± 1.2 vol.%.
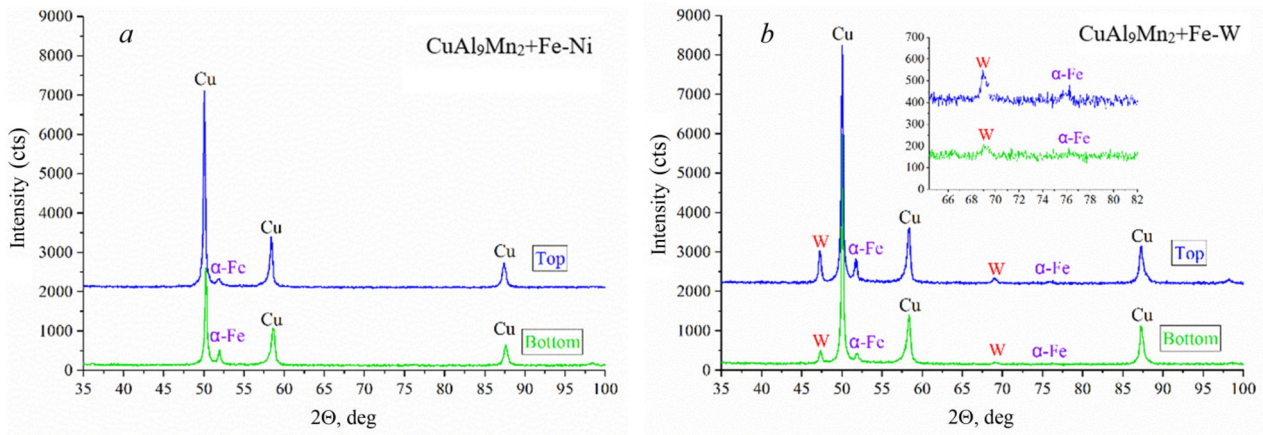
Fig. 4. X-ray radiographs obtained from the bottom and top parts of CuAl$_9$Mn$_2$ + Fe–Ni (*a*) and CuAl$_9$Mn$_2$ + Fe–W composites (*b*).
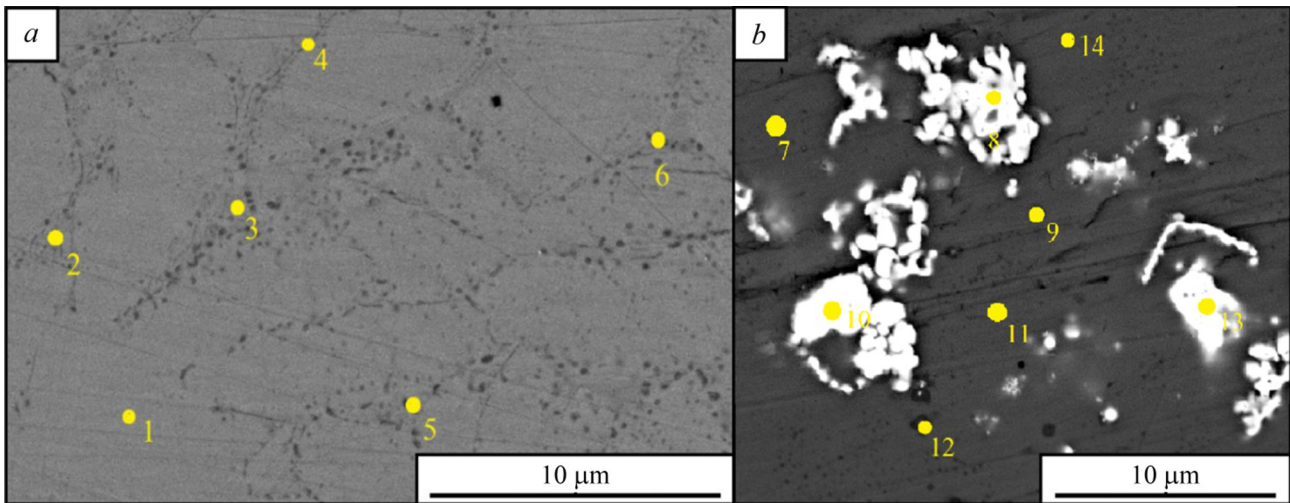

Fig. 5. SEM images of CuAl$_9$Mn$_2$ + Fe–Ni microstructure (*a*) and CuAl$_9$Mn$_2$ + Fe–W (*b*) obtained by EBAM method; the numbered points indicate the EDS analysis locations.

In the case of CuAl$_9$Mn$_2$ + Fe–W composite with addition of a mixture of iron and tungsten powders, two lattices belonging to BCC iron and tungsten and one lattice of FCC copper were detected by XRD. In this case, the content of α-Fe and W was 5.7 ± 0.3 vol. % and 6.6 ± 1.4 vol. %, respectively.

Nevertheless, under unsteady conditions of melting and crystallization of the studied systems, new phases should arise. This fact is confirmed by SEM studies below and by the absence of multicomponent phases in the XRD analysis: we can conclude that the content of these phases is less than 3–5% (XRD limit).

Fig. 5*a* shows the microstructure of CuAl$_9$Mn$_2$ + Fe–Ni composite, which is characterized by the presence of α-Cu represented by light gray color surrounded by Cu$_3$Al according to the spectra 2-6 EDS analysis presented in Table 4. Tao *et al*. [11] showed that as the iron and nickel content of aluminum bronze increases, it solidifies into a solid copper solution, which leads to lattice distortion. The fast cooling rate characteristic of EBAM printing contributes to the formation of the martensitic β'-phase from the β-phase, as shown in [13]. The microstructure of the CuAl$_9$Mn$_2$ + Fe–W composite in Fig. 5*b* is represented by bronze matrix (spectra 11 and 13 in Table 4) with large dispersed particles of W–Si system (spectra 8, 10, and 13 in Table 4).

TABLE 4. EDS Analysis of the Obtained $CuAl_9Mn_2$ + Fe–Ni (*a*) and $CuAl_9Mn_2$ + Fe–W Composites (*b*) (Fig. 5)

Spectrum	Chemical composition, at.%									System/phase
	Al	Si	Cr	Mn	Fe	Co	Ni	Cu	W	
1	14.9	–	0.2	0.8	2.9	0.2	2.8	78.2	–	α-Cu
2	18.9	–	0.1	0.8	2.5	0.2	3.5	74.9	–	
3	21.4	–	0.1	0.9	2.4	0.1	4.1	70.9	–	
4	16.1	–	0.4	1.1	2.8	0.3	3.3	76.0	–	Cu_3Al
5	20.9	0.2	0.1	0.9	3.1	0.1	4.9	69.8	–	
6	21.4	–	0.1	0.9	2.0	0.1	3.6	71.9	–	
7	16.7	–	0.4	1.3	3.4	0.3	0.4	77.2	0.3	Cu3Al
8	5.6	16.7	1.1	1.1	9.7	0.5	0.8	18.3	46.1	W–Si
9	13.9	1.2	1.0	1.6	44.9	0.6	0.7	35.9	0.3	Cu–Fe–Al
10	4.9	21.9	1.9	1.4	2.5	1.0	1.2	9.0	56.2	W–Si
11	15.4	–	0.3	1.1	3.5	0.1	0.4	79.3	–	α-Cu
12	14.6	1.5	0.8	1.5	47.5	0.3	0.5	31.3	2.0	Cu–Fe–Al
13	4.6	20.1	1.9	1.2	8.2	1	1.1	7.9	53.9	W–Si
14	14.8	–	0.3	1.1	3.4	0.2	0.4	79.9	–	α-Cu
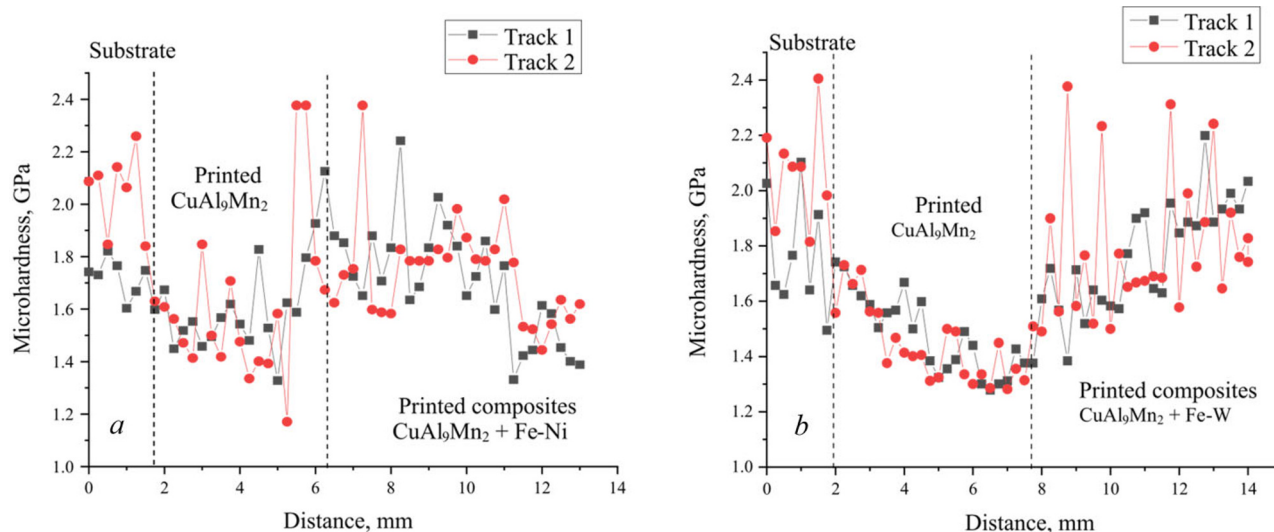
Fig. 6. Microhardness profiles of $CuAl_9Mn_2$ + Fe–Ni (*a*) and $CuAl_9Mn_2$ + Fe–W composites (*b*) obtained by the EBAM method.

The results of microhardness measurements of the $CuAl_9Mn_2$ + Fe–Ni and $CuAl_9Mn_2$ + Fe–W composites measured in the perpendicular section with respect to the print are shown in Fig. 6. The initial values in both composites are characterized by substrate hardness values of 2.0 ± 0.2 GPa. The printed part of the $CuAl_9Mn_2$ alloy tends to decrease the hardness values from 1.8 to 1.2 GPa, which is caused by a decrease in the steel substrate material mixed into the bronze matrix. The printed $CuAl_9Mn_2$ + Fe–Ni composite shows a jump-like character of hardness change with its gradual decrease closer to the surface. The highest values reached 2.4 ± 0.2 GPa, which is associated with hardening of the copper-based solid solution (Fig. 6*a*). In Fig. 6*b*, in the region of the printed $CuAl_9Mn_2$ + Fe–W composite, the

TABLE 5. Tensile Characteristics for $CuAl_9Mn_2 + Fe–Ni$ and $CuAl_9Mn_2 + Fe–W$ Composite Samples Printed by EBAM

Composite	Cutout direction	Yield stress, MPa	Tensile stress, MPa	Relative elongation, %
$CuAl_9Mn_2 + Fe–Ni$	Longitudinal	402	741	29
	Transverse	361	713	35
$CuAl_9Mn_2 + Fe–W$	Longitudinal	295	667	33
	Transverse	327	700	34
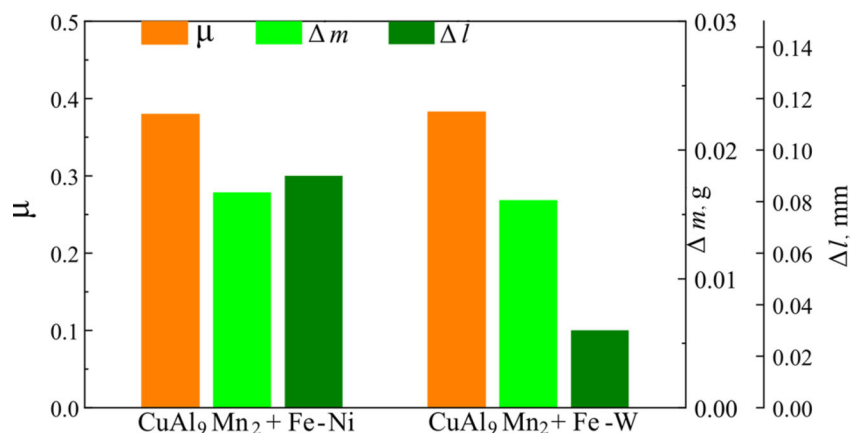
Fig. 7. Tribological characteristics of $CuAl_9Mn_2 + Fe–Ni$ and $CuAl_9Mn_2 + Fe–W$ composites.

microhardness values increased irregularly up to the sample surface. The peaks showing hardness values of 2.4 ± 0.1 GPa refer to agglomerates of tungsten and iron powders presented in the bronze matrix (Fig. 3c and d).

The mechanical tests of $CuAl_9Mn_2 + Fe–Ni$ and $CuAl_9Mn_2 + Fe–W$ composites in the transverse and longitudinal directions showed that the maximum strength was achieved in the longitudinal samples of $CuAl_9Mn_2 + Fe–Ni$ composite when the tensile axis coincided with the printing direction (Table 5). In the $CuAl_9Mn_2 + Fe–W$ composite, the maximum strength in the transverse direction was 700 MPa. For a comparison, the tensile strength of pure $CuAl_9Mn_2$ bronze after electron beam printing s about 435–483 MPa depending on the orientation of the sample cutout [13]. Composite materials are significantly superior to pure electron beam printed bronze in strength and yield stress, but the ductility of the materials is expected to decrease by 2 times compared to $CuAl_9Mn_2$ bronze.

Tribological tests of the obtained samples showed sufficiently high wear resistance of both types of the formed materials (Fig. 7). Close values of friction coefficients of the order of 0.37–0.38 were characteristic for both composites. Mass wear was also at close levels. However, the linear wear of the sample with the addition of tungsten and iron powder was 3 times lower than that of the sample with the introduction of nickel and iron. This shows the greater influence of plastic displacement of the material from the friction zone for samples with the introduction of nickel and iron, which is a negative factor in terms of serviceability of the product in the friction node.

CONCLUSIONS

The performed work has demonstrated a high degree of applicability of the electron beam additive manufacturing technology for obtaining composite materials based on $CuAl_9Mn_2$ bronze with the addition of Fe–Ni and Fe–W powder compositions during printing. The structure of the samples did not show the presence of pores, cracks or delaminations. The main defects were powder agglomerates of small size (up to 100 μm). In the main volume, the

powder material was distributed quite evenly, which leads to high strength characteristics of the samples. The increase of strength characteristics from 435–483 MPa for pure bronze to 667–741 MPa and up to twofold increase of wear resistance for the composite samples also allowed increasing tribological properties of the composites. The greatest wear resistance was characteristic for samples with Fe–W addition, the lower values were demonstrated by samples with Fe–Ni addition.

REFERENCES

1. S. Munje, S. Kulkarni, V. Vatsal, *et al.*, Mater. Today Proc., **61**, 303–312 (2022).
2. F. Dababneh and H. Taheri, CIRP J. Manuf. Sci. Technol., **38**, 706–716 (2022).
3. E. A. Kolubaev, V. E. Rubtsov, A. V. Chumaevsky, and E. G. Astafurova, Phys. Mesomech., **25**, No. 6, 479–491 (2022).
4. H. S. Fiaz, C. R. Settle, and K. A. Hoshino, Sens. Actuators A Phys. **249**, 284–293 (2016).
5. J. Zhang, Q. Cao, and W. F. Lu, Mater. Today Proc., **70**, 407–411 (2022).
6. M. Dias, J. P. M. Pragana, B. Ferreira, et al., Sustainability, **14 (9)**, 5197 (2022).
7. X. Liu, D. Huang, C. Yan, *et al.*, Mater. Charact., **167**, 110511 (2020).
8. H. Ye, A. Chen, S. Liu, *et al.*, Surf. Coatings Technol., **433**, 128126 (2022).
9. X. J. Ho, A. Saulot, M. Busquet, *et al.*, Tribol. Int. **65**, 354–362 (2013).
10. S. Nair, R. Sellamuthu, and R. Saravanan, Mater. Today Proc. **5**, 6617–6625 (2018).
11. X. P. Tao, S. Zhang, C. H. Zhang, *et al.*, Surf. Coatings Technol. **342**, 76–84 (2018).
12. A. P. Zykova, A. V. Chumaevskii, A. O. Panfilov, *et al.*, Materials (Basel). **15**, 6270 (2022).
13. A. P. Zykova, A. O. Panfilov, A. V. Chumaevskii, *et al.*, Russ. Phys. J. **65**, 811–817 (2022).